2016 IEEE International Conference on Robotics and Automation (ICRA)
Stockholm, Sweden, May 16-21, 2016

Extending *kalibr*: Calibrating the Extrinsics of Multiple IMUs and of Individual Axes

Joern Rehder, Janosch Nikolic, Thomas Schneider, Timo Hinzmann and Roland Siegwart[1]

Abstract— **An increasing number of robotic systems feature multiple inertial measurement units (IMUs). Due to competing objectives—either desired vicinity to the center of gravity when used in controls, or an unobstructed field of view when integrated in a sensor setup with an exteroceptive sensor for ego-motion estimation—individual IMUs are often mounted at considerable distance. As a result, they sense different accelerations when the platform is subjected to rotational motions. In this work, we derive a method for spatially calibrating multiple IMUs in a single estimator based on the open-source camera/IMU calibration toolbox *kalibr*. We further extend the toolbox to determine IMU intrinsics, enabling accurate calibration of low-cost IMUs. The results suggest that the extended estimator is capable of precisely determining these intrinsics and even of localizing individual accelerometer axes inside a commercial grade IMU to millimeter precision.**

I. Introduction

With the costs for inertial measurement units steadily declining and the emergence of integrated visual/inertial sensors, an increasing number of robotics platforms feature multiple inertial measurement units. An example for such a system is the Boston Dynamics quadrupedal platform [1] equipped with a tactical grade IMU rigidly mounted to a stereo camera setup and used for visual/inertial odometry and with a navigation grade IMU positioned inside the body of the robot. Another example is the quadrotor platform by Shen et al. [2], which employs a low-cost IMU for low-level controls in the autopilot and an additional, high-performance IMU for visual/inertial motion estimation. These platforms have in common that they employ a main IMU positioned and aligned in a way meaningful for locomotion (i.e. mounted close the center of gravity and aligned with the main axes of the platform) and a second, auxiliary IMU mounted in the vicinity of some exteroceptive sensors in a location with minimal obstruction by the platform itself. For most platforms, these two locations will be vastly different. In order to make sense of ego-motion estimates from the auxiliary sensor suite for controls and locomotion, they will have to be transformed to the coordinate frame of the main IMU. To this end, an accurate estimate of the transformation between the two coordinate frames is required.

While it is possible to estimate the transformation of both IMUs with respect to the exteroceptive sensor and subsequently chain them, little work presents on fusion of measurements from multiple IMUs inside a single estimator. We suspect one of the reasons for this to lie in the fact that angular accelerations are required to model accelerations perceived in any location outside the accelerometer input axes (IA)—a quantity that is often not measured directly.[1] While it would be possible to derive an estimate of angular acceleration from numerically differentiating angular velocity measurements perceived by the gyroscopes, we pursued a different approach here: The well-established continuous-time batch estimation framework presented by Furgale et al. [5] fits a spline representing the evolution of the relative orientation of two coordinate frames over time to a series of orientation and angular velocity measurements. Assuming that angular velocity varies smoothly, an estimate of angular acceleration can be directly derived from this orientation curve.

The same estimator enables further applications: High-end IMUs often employ one integrated circuit (IC) per axis for acceleration measurements rather than a single IC that combines all axes on a single die. Individual axes may be multiple centimeters apart, which violates the assumption that they are subject to the same acceleration under general motion. If unaccounted for, this introduces errors which are sometimes referred to as the "size effect" in the navigation literature [6]. Consequently, the offsets of individual axes to the origin of the input reference axes (IRA) should be considered for maximum calibration performance.

The contributions of this work are the following:

- We derive an estimator for simultaneous intrinsic and extrinsic calibration of multiple IMUs with respect to one or multiple exteroceptive sensors.
- We generalize this estimator to additionally determine the location of individual accelerometer axes.
- We present a comprehensive experimental study demonstrating precise intrinsic calibration and showing that it is possible to locate individual accelerometer axes inside a commercial grade IMU.

The approach was implemented as an extension to the open-source camera/IMU calibration toolbox *kalibr*[2] [7] and will be released as an update to it.

II. Related Work

This work is concerned with calibrating a sensor suite comprising one or multiple IMUs and one or multiple extero-

[1] All authors are with the ETH, the Swiss Federal Institute of Technology Zurich, Autonomous Systems Lab (www.asl.ethz.ch), Leonhardstrasse 21, LEE, CH-8092 Zurich, Switzerland. {joern.rehder, janosch.nikolic, timo.hinzmann}@mavt.ethz.ch, rsiegwart@ethz.ch.

[1] There exist different approaches for measuring angular accelerations, a not so recent review of which is provided in [3]. More recently, consumer grade MEMS angular acceleration sensors have been announced [4]. However, these devices are currently not widely employed.

[2] https://github.com/ethz-asl/kalibr

TABLE I

		Estimated Quantities							
	Estimation Approach	$\mathbf{S}_{\alpha,\omega}$	$\mathbf{M}_{\alpha,\omega}$	$\mathbf{A}_{\omega}$	${}_B\mathbf{r}_{BA}$	$\mathbf{C}_{BC}, {}_B\mathbf{r}_{BC}$	d_c	**fc**, **cc**, **kc**	$\mathbf{b}_{\alpha,\omega}$
Mirzaei [8], Kelly [9], [10]	EKF					•	•*		•
Fleps [11], Mair [12]	cont.-time batch optimization					•	•*		•
Furgale [7]	cont.-time batch optimization					•	•		•
Zachariah [13]	SPKF	•	•	•		•			•
Li [14]	MSCKF	•	•	•		•	•	•	•
Krebs [15]	cont.-time batch optimization	•	•	•		•	•		•
Ours	cont.-time batch optimization	•	•	•	•	•	•		•

ceptive sensors. The goal of the calibration is to improve state estimation results obtained from fusing measurements from *all* sensors available. Accordingly, estimating the extrinsics of the IMUs with respect to an exteroceptive sensor is an integral part of the approach, and we will limit the review of related work to approaches similar in scope.

Nevertheless, there exists a large body of work addressing the problem of calibrating redundant IMUs for applications where fusion with additional sensors is not a focus. Possible starting points for further literature review in this direction could be the work by Pittelkau [16], Hwangbo et al. [17], and Nilsson et al. [18].

Mirzaei et al. [8] and Kelly et al. [9] proposed an extended Kalman filter (EKF)-based framework that estimated the transformation between an IMU and a camera from a calibration sequence recorded by moving the setup in front of a visual target. Using a similar calibration procedure, Fleps et al. [11] determined these quantities by means of batch optimization. Their approach estimated a continuous trajectory encoded as a spline rather than representing the motion as a discrete sequence of states. Furgale et al. [7] pursued a similar continuous-time approach, but additionally folded the estimation of a temporal offset between camera and IMU into the estimator—a parameter that had previously been estimated in a separate procedure ([10], [12]). Krebs extended the approach by IMU intrinsics [15]. Similarly, Zachariah et al. [13] incorporated intrinsic parameters into a discrete-time sigma-point Kalman filter (SPKF) estimation framework. Recently, Li et al. [14] demonstrated the estimation of camera/IMU extrinsics, a time delay and IMU intrinsics as an integral part of an online state estimation framework using a multi-state-constraint Kalman filter (MSCKF). In contrast to other methods reviewed here, their approach uses natural visual landmarks rather than a dedicated calibration pattern and additionally estimates the camera intrinsic parameters focal length **fc**, principle point **cc** and distortion parameters **kc**.

Our approach is based on [7] and extends that method to incorporate multiple IMUs into a single estimator. The same formulation can be employed to determine the displacement of individual accelerometer axes, arriving at a more complete model even in sensor suites comprising only a single IMU. Borrowing from [15], IMU intrisics were added to the calibration parameters to improve results.

Table I summarizes these approaches using the notation that will be introduced in Section III-D. Asterisks mark approaches where temporal calibration is performed in a separate, preceding step.

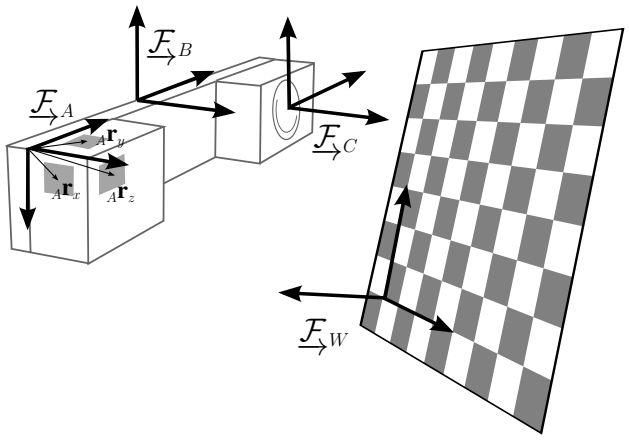

Fig. 1: Coordinate frame convention. $\underrightarrow{\mathcal{F}}_W$ denotes the world reference frame, and $\underrightarrow{\mathcal{F}}_B$ and $\underrightarrow{\mathcal{F}}_A$ mark the input reference axes (IRA) and the eccentric IMU frame respectively. A camera was used as exteroceptive sensor, denoted here with $\underrightarrow{\mathcal{F}}_C$. $\underrightarrow{\mathcal{F}}_B$, $\underrightarrow{\mathcal{F}}_C$ and $\underrightarrow{\mathcal{F}}_A$ are connected through a rigid mechanical link. Gray boxes mark the locations of individual accelerometer ICs, which are displaced with respect to $\underrightarrow{\mathcal{F}}_A$ by individual lever arms ${}_A\mathbf{r}_{x,y,z}$. For simplicity, we will assume ${}_A\mathbf{r}_x = \mathbf{0}$ in the following.

III. Method

A. Coordinate frame conventions

Fig. 1 visualizes the different coordinate frames used in this work. The inertial frame $\underrightarrow{\mathcal{F}}_W$ is attached to the calibration pattern. $\underrightarrow{\mathcal{F}}_B$ marks the body IRA, while $\underrightarrow{\mathcal{F}}_A$ and $\underrightarrow{\mathcal{F}}_C$ denote the IMU frame and the frame of the exteroceptive sensor respectively. $\underrightarrow{\mathcal{F}}_B$, $\underrightarrow{\mathcal{F}}_C$ and $\underrightarrow{\mathcal{F}}_A$ are rigidly connected through a mechanical link. We will estimate the time-varying relative orientation and position of $\underrightarrow{\mathcal{F}}_B$ with respect to $\underrightarrow{\mathcal{F}}_W$.

In order for the IRA to be well defined in practice, the spatial offset to at least one axis of at least one IMU needs to be fixated. This could be an arbitrary displacement, but

for convenience, we choose to align the IRA with one IMU when calibrating with multiple devices, and the x-axis of the IRA with the accelerometer sensing the specific force in x direction when calibrating for displacements of individual axes (i.e. ${}_A\mathbf{r}_x = \mathbf{0}$).

B. Accelerometer model

Here, we will derive the model of inertial measurements used for calibration in the estimator.

Let ${}_W\mathbf{t}_{WB}(t)$ denote the time-varying vector from the origin of coordinate frame $\underrightarrow{\mathcal{F}}_W$ to coordinate frame $\underrightarrow{\mathcal{F}}_B$ expressed in $\underrightarrow{\mathcal{F}}_W$. With this, the acceleration of the origin of coordinate frame $\underrightarrow{\mathcal{F}}_B$ expressed in $\underrightarrow{\mathcal{F}}_W$ is given by ${}_W\ddot{\mathbf{t}}_{WB}(t)$.

The measurements of an ideal accelerometer (i.e. the specific force) at coordinate frame $\underrightarrow{\mathcal{F}}_B$ can be expressed as

$$ {}_B\mathbf{a}_{WB}(t) = \mathbf{C}_{BW}(t)\left({}_W\ddot{\mathbf{t}}_{WB}(t) - {}_W\mathbf{g}\right) \tag{1} $$

where $\mathbf{C}_{BW}(t)$ denotes the time-varying direction cosine matrix that transforms a vector from $\underrightarrow{\mathcal{F}}_W$ to $\underrightarrow{\mathcal{F}}_B$, and ${}_W\mathbf{g}$ marks the gravitational force.

Now assume that we would like to model the acceleration of a coordinate frame $\underrightarrow{\mathcal{F}}_A$, rigidly attached to $\underrightarrow{\mathcal{F}}_B$ with constant displacement ${}_B\mathbf{r}_{BA}$. The temporal evolution of the origin of this coordinate frame, expressed in $\underrightarrow{\mathcal{F}}_W$, is given by ${}_W\mathbf{t}_{WA} = {}_W\mathbf{t}_{WB}(t) + \mathbf{C}_{BW}^T(t){}_B\mathbf{r}_{BA}$. Accordingly, ${}_A\mathbf{a}_{WA}(t)$ is given by

$$ \begin{aligned} {}_A\mathbf{a}_{WA}(t) = \mathbf{C}_{AB}^{\alpha}(&\mathbf{C}_{BW}(t)({}_W\ddot{\mathbf{t}}_{WB}(t) - {}_W\mathbf{g}) \\ &+ \lfloor {}_B\dot{\boldsymbol{\omega}}_{WB}(t)\rfloor_\times {}_B\mathbf{r}_{BA} \\ &+ \lfloor {}_B\boldsymbol{\omega}_{WB}(t)\rfloor_\times^2 {}_B\mathbf{r}_{BA}) \end{aligned} \tag{2} $$

where $\mathbf{C}_{AB}^{\alpha}$ marks the rotation matrix relating $\underrightarrow{\mathcal{F}}_A$ and $\underrightarrow{\mathcal{F}}_B$, ${}_B\boldsymbol{\omega}_{WB}(t)$ denotes the angular velocity of $\underrightarrow{\mathcal{F}}_W$ with respect to $\underrightarrow{\mathcal{F}}_B$ and ${}_B\dot{\boldsymbol{\omega}}_{WB}(t)$ denotes the angular acceleration. The operator $\lfloor\cdot\rfloor_\times$ denotes the skew-symmetric matrix expressing the cross products.

In the most simplistic accelerometer model, we assume that the accelerometer input axes (IA) are aligned with $\underrightarrow{\mathcal{F}}_A$ and that the accelerometer measurements $\boldsymbol{\alpha}(t)$ are only affected by noise:

$$ \boldsymbol{\alpha}(t) = {}_A\mathbf{a}_{WA}(t) + \mathbf{b}_\alpha(t) + \boldsymbol{\nu}_\alpha \tag{3a} $$

$$ \dot{\mathbf{b}}_\alpha(t) = \boldsymbol{\nu}_{b\alpha} \tag{3b} $$

where $\boldsymbol{\nu}_\alpha$ and $\boldsymbol{\nu}_{b\alpha}$ are zero-mean, white Gaussian noise processes of strength $\sigma_\alpha^2\mathbf{I}$ and $\sigma_{b\alpha}^2\mathbf{I}$. In other words, the accelerometer measurements are independently affected by white noise $\boldsymbol{\nu}_\alpha$ and a slowly varying random walk process of diffusion $\sigma_{b\alpha}^2\mathbf{I}$, $\mathbf{b}_\alpha(t)$.

This model is a good approximation for devices with factory calibrated intrinsics, but may produce impaired calibration results for low-cost, consumer grade inertial sensors which exhibit significant axis misalignment and scale factor errors. Hence, for these sensors, the model is augmented to include misalignment and incorrect scales:

$$ \boldsymbol{\alpha}(t) = \mathbf{S}_\alpha\mathbf{M}_{\alpha A}{}_A\mathbf{a}_{WA}(t) + \mathbf{b}_\alpha(t) + \boldsymbol{\nu}_\alpha \tag{4} $$

where $\mathbf{S}_\alpha$ is a diagonal matrix comprising scaling effects and $\mathbf{M}_\alpha$ is a lower unitriangular matrix, with lower off-diagonal elements corresponding to misalignment small angles.

Equation 5 can be extended to accommodate a design trait common to many high-end IMUs: These often employ an individual sensor IC per measurement axis, and there are physical limits on the proximity in which the sensors can be mounted. Consequently, *each axis* is displaced differently from the input reference axes (IRA). With $\boldsymbol{\omega}(t) := {}_B\boldsymbol{\omega}_{WB}(t), \dot{\boldsymbol{\omega}}(t) := {}_B\dot{\boldsymbol{\omega}}_{WB}(t)$, the complete model with individually displaced accelerometer axes amounts to

$$ \begin{aligned} {}_A\mathbf{a}_{WA}(t) =&\mathbf{C}_{AB}^{\alpha}(\mathbf{C}_{BW}(t)({}_W\ddot{\mathbf{t}}_{WB}(t) - {}_W\mathbf{g}) \\ &+ \operatorname{diag}(\lfloor\dot{\boldsymbol{\omega}}(t)\rfloor_\times\mathbf{R}_\alpha + \lfloor\boldsymbol{\omega}(t)\rfloor_\times^2\mathbf{R}_\alpha)), \end{aligned} \tag{5} $$

where $\operatorname{diag}(\cdot)$ extracts the $N\times 1$ vector from the diagonal of a matrix and $\mathbf{R}_\alpha$ is composed of the lever arms of individual accelerometers (identified by the subscripts) according to

$$ \mathbf{R}_\alpha = \begin{bmatrix} {}_B\mathbf{r}_{BA_x} & {}_B\mathbf{r}_{BA_y} & {}_B\mathbf{r}_{BA_z} \end{bmatrix}. \tag{6} $$

C. Gyroscope model

Analogously, given the angular velocity ${}_B\boldsymbol{\omega}_{WB}$ governing the time-varying change in orientation between $\underrightarrow{\mathcal{F}}_B$ and $\underrightarrow{\mathcal{F}}_W$ expressed in $\underrightarrow{\mathcal{F}}_B$, the angular velocity expressed in $\underrightarrow{\mathcal{F}}_A$ is given as

$$ {}_A\boldsymbol{\omega}_{WB}(t) = \mathbf{C}_{AB}^{\omega}{}_B\boldsymbol{\omega}_{WB}(t) \tag{7} $$

The rationale behind estimating $\mathbf{C}_{AB}^{\omega}$ and $\mathbf{C}_{AB}^{\alpha}$ separately lies in sensor imperfections: The gyroscopes may not be perfectly aligned with the accelerometers, and estimating a single $\mathbf{C}_{AB}$ would in turn be a source of deterministic errors in the model.

Again, a properly factory calibrated gyroscope can be modelled as

$$ \boldsymbol{\varpi}(t) = {}_A\boldsymbol{\omega}_{WB}(t) + \mathbf{b}_\omega(t) + \boldsymbol{\nu}_\omega \tag{8a} $$

$$ \dot{\mathbf{b}}_\omega(t) = \boldsymbol{\nu}_{b\omega} \tag{8b} $$

where $\boldsymbol{\nu}_\omega$ and $\boldsymbol{\nu}_{b\omega}$ are zero-mean, white Gaussian noise processes of strength $\sigma_\omega^2\mathbf{I}$ and $\sigma_{b\omega}^2\mathbf{I}$, i.e. the gyroscopes are independently affected by white noise and a random walk process, analogously to the accelerometers.

For consumer grade devices, the influence of axis misalignment and incorrect measurement scaling as well as of linear accelerations on gyroscope measurements ("g-sensitivity") can be modelled as

$$ \boldsymbol{\varpi}(t) = \mathbf{S}_\omega\mathbf{M}_{\omega A}{}_A\boldsymbol{\omega}_{WB}(t) + \mathbf{A}_{\omega A}{}_A\mathbf{a}_{WA}(t) + \mathbf{b}_\omega(t) + \boldsymbol{\nu}_\omega \tag{9} $$

where $\mathbf{S}_\omega$ and $\mathbf{M}_\omega$ are defined analogously to $\mathbf{S}_\alpha$ and $\mathbf{M}_\alpha$ in (4), and $\mathbf{A}_\omega$ is a fully populated matrix. Despite presumably having different displacements from the IRA, only a single lever arm is considered in the calculation of ${}_A\mathbf{a}_{WA}(t)$. In general, the effect of linear accelerations on gyroscope measurements is small and insufficient to properly constrain the estimate of a spatial displacement. In this work, we assume the accelerometer and gyroscopes to be sufficiently close and employ the lever arm estimated for the accelerometers. In cases where an individual lever arm per accelerometer axis

is determined, the estimate of one axis is employed for all axes of the gyroscope.

D. The estimator

So far, we established the basis for modelling accelerometer and gyroscope measurements from devices mounted with an offset to the IRA. Generally, these models could be employed in any estimator. However, both, (5) and, to a lesser extent, (9), depend on angular accelerations, and this quantity is not measured directly in most sensor suites. Accordingly, it has to be inferred, and we employ the continuous-time batch optimization paradigm [5], which estimates a continuously differentiable sensor trajectory, yielding a smooth estimate of angular accelerations.

In the following, we will give a brief introduction to continuous-time estimation, which will follow Furgale et al. [7] very closely. For a more thorough derivation, please see the original publication [5].

Time-varying states are represented as the weighted sum of a finite number of known analytical basis functions. For example, a D-dimensional state, $\mathbf{x}(t)$, may be written as

$$\mathbf{\Phi}(t) := \begin{bmatrix}\phi_1(t) & \dots & \phi_B(t)\end{bmatrix}, \quad \mathbf{x}(t) := \mathbf{\Phi}(t)\mathbf{c}, \tag{10}$$

where each $\phi_b(t)$ is a known $D \times 1$ analytical function of time and $\mathbf{\Phi}(t)$ is a $D \times B$ stacked basis matrix. We estimate $\mathbf{x}(t)$ by determining $\mathbf{c}$, a $B \times 1$ vector of coefficients.

While various basis functions are feasible, we employ B-splines due to their simple analytical derivatives, good representational power and finite temporal support, yielding a sparse system of equations in the estimator that can be solved efficiently.

The pose of $\underrightarrow{\mathcal{F}}_B$ is parameterized as a 6×1 spline with 3 degrees of freedom for relative translation and 3 degrees of freedom for relative orientation:

$${}_W\mathbf{t}_{WB}(t) := \mathbf{\Phi}_t(t)\mathbf{c}_t \tag{11}$$

$$\boldsymbol{\varphi}(t) := \mathbf{\Phi}_\varphi(t)\mathbf{c}_\varphi\,. \tag{12}$$

In this paper, we use the axis/angle parameterization for rotations, where $\boldsymbol{\varphi}(t)$ represents rotation by the angle $\varphi = \sqrt{\boldsymbol{\varphi}(t)^T\boldsymbol{\varphi}(t)}$ about the axis $\boldsymbol{\varphi}(t)/\varphi(t)$. The orientation of $\underrightarrow{\mathcal{F}}_W$ with respect to $\underrightarrow{\mathcal{F}}_B$ at time t is given by $\mathbf{C}_{BW}(t) := \boldsymbol{\mathcal{C}}\big(\boldsymbol{\varphi}(t)\big)^T$, where $\boldsymbol{\mathcal{C}}(\cdot)$ is a function that builds a direction cosine matrix from the orientation parameters $\boldsymbol{\varphi}(t)$.

Acceleration ${}_W\ddot{\mathbf{t}}_{WB}(t)$ is computed as

$${}_W\ddot{\mathbf{t}}_{WB}(t) = \ddot{\mathbf{\Phi}}_t(t)\mathbf{c}_t \tag{13}$$

from the spline parameters $\mathbf{c}_t$.

Angular velocity and angular acceleration as perceived in $\underrightarrow{\mathcal{F}}_B$ are computed as

$${}_B\boldsymbol{\omega}_{WB}(t) = \mathbf{C}_{BW}(t)\ {}_W\boldsymbol{\omega}_{WB}(t) \tag{14}$$

$${}_B\dot{\boldsymbol{\omega}}_{WB}(t) = \mathbf{C}_{BW}(t)\ {}_W\dot{\boldsymbol{\omega}}_{WB}(t) \tag{15}$$

with

$${}_W\boldsymbol{\omega}_{WB}(t) = \mathbf{S}\big(\boldsymbol{\varphi}(t)\big)\dot{\boldsymbol{\varphi}}(t) = \mathbf{S}\big(\mathbf{\Phi}(t)\mathbf{c}_\varphi\big)\dot{\mathbf{\Phi}}(t)\mathbf{c}_\varphi \tag{16}$$

$${}_W\dot{\boldsymbol{\omega}}_{WB}(t) = \mathbf{S}\big(\boldsymbol{\varphi}(t)\big)\ddot{\boldsymbol{\varphi}}(t) = \mathbf{S}\big(\mathbf{\Phi}(t)\mathbf{c}_\varphi\big)\ddot{\mathbf{\Phi}}(t)\mathbf{c}_\varphi \tag{17}$$

where $\mathbf{S}(\cdot)$ is the matrix relating parameter rates to angular velocities and accelerations [19].

For both, orientation and translation, a sixth-order B-spline is employed, which encodes linear and angular acceleration as a cubic polynomial.

Time-varying sensor biases are represented by cubic B-splines:

$$\mathbf{b}(t) := \mathbf{\Phi}_b(t)\mathbf{c}_b \tag{18}$$

The estimator further requires inputs from exteroceptive sensors to sufficiently constrain the trajectory. This can be any sensor that acquires measurements sufficient to render all quantities of interest observable. Since this work is an extension of *kalibr*, we employed a global shutter camera with a static calibration pattern for this purpose.

Projections of reference points on the calibration pattern ${}_W\mathbf{p}^i$ are modelled according to the well-established pinhole camera model

$$\begin{aligned}\mathbf{y}_k^i = f(&\mathbf{C}_{BC}^T(\mathbf{C}_{BW}(t_k + d_c)\left({}_W\mathbf{p}^i + {}_W\mathbf{t}_{WB}(t_k + d_c)\right)\\ &+ {}_B\mathbf{r}_{BC})) + \boldsymbol{\nu}_y \quad ,\end{aligned} \tag{19}$$

where the function $f(\cdot)$ denotes a perspective projection. d_c is an unknown relative temporal offset that compensates for either the IMU or the camera assigning timestamps with a fixed offset with respect to their measurement instant. We assume that the projections are corrupted in the image plane by a zero-mean, discrete-time, white Gaussian noise process of variance $\sigma_y^2\mathbf{I}$.

The estimator is formulated as a non-linear least-square optimization problem. Our previously introduced measurement models ((4), (9), and (19)) are all of the form $\mathbf{m}(t) := h(\mathbf{\Theta}, t) + \boldsymbol{\nu}$, where $\mathbf{\Theta}$ is a vector containing all estimated quantities, t denotes the instant at which the measurement was recorded and the model is evaluated, and $\boldsymbol{\nu}$ is a zero-mean, white Gaussian noise process of strength $\sigma^2\mathbf{I}$. Accordingly, the contribution of measurements $\tilde{\mathbf{m}}_k^i$ recorded with sensor i at times $[t_1, \dots, t_N]$ to the objective function J can be formulated as

$$J_i := \sum_{k=1}^{N} \frac{1}{\sigma_i^2}\left|\tilde{\mathbf{m}}_k^i - h^i(\mathbf{\Theta}, t_k)\right|^2. \tag{20}$$

Contributions from bias terms are evaluated according to

$$J_b := \int_{t_1}^{t_N} \frac{1}{\sigma_b^2}\left|\dot{\mathbf{b}}(\tau)\right|^2 \mathrm{d}\tau. \tag{21}$$

The objective function is composed from these sensor and bias terms, and the estimate is determined as the $\mathbf{\Theta}$ that minimizes J:

$$\mathbf{\Theta} = \underset{\mathbf{\Theta}}{\operatorname{argmin}}\left(J_\alpha + J_\varpi + J_y + J_{b_\alpha} + J_{b_\omega}\right). \tag{22}$$

We employ the Levenberg-Marquardt algorithm [20] for non-linear optimization.

The following table lists the parameters and states comprised in $\mathbf{\Theta}$ and partitions them into time-varying and time-invariant, and IMU and "auxiliary" parameters.

	Time-Invariant
$\mathbf{C}_{AB}^{\alpha}$	orientation of the accelerometers
$\mathbf{C}_{AB}^{\omega}$	orientation of the gyroscopes
${}_B\mathbf{r}_{BA}$	displacement of the IMU
$\mathbf{S}_{\alpha}$	accelerometer scale factors
$\mathbf{M}_{\alpha}$	accelerometer misalignment
$\mathbf{S}_{\omega}$	gyroscope scale factors
$\mathbf{M}_{\omega}$	gyroscope misalignment
$\mathbf{A}_{\omega}$	effect of linear accelerations on gyroscopes
$\mathbf{C}_{BC}$	orientation of the camera
${}_B\mathbf{r}_{BC}$	displacement of the camera
d_c	temporal offset between IMU and camera
${}_W\mathbf{g}$	direction of gravity
	Time-Varying
${}_W\mathbf{t}_{WB}$	position of the IRA expressed in $\underrightarrow{\mathcal{F}}_W$
$\boldsymbol{\varphi}$	orientation parameters of the IRA
$\mathbf{b}_a$	accelerometer bias
$\mathbf{b}_{\omega}$	gyroscope bias

IV. Experiments

A. Experimental setup and dataset collection

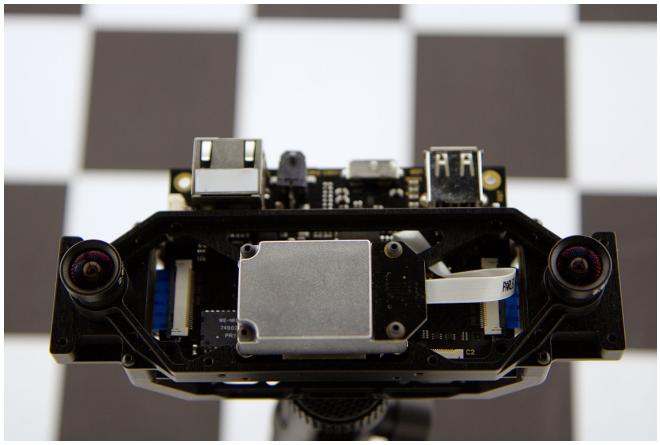

Fig. 2: The experimental setup used in this work. The integrated visual/inertial sensor [21] is equipped with two global shutter image sensors, as well as three MEMS IMUs. A factory calibrated Analog Devices ADIS16448 is mounted centrally on the sensor frame; the two consumer grade Invensense MPU9150 IMUs are located on the back of each image sensor board.

For our experiments, we employed a visual/inertial sensor [21], which was equipped with an Analog Devices ADIS16448 and two Invensense MPU9150 IMUs. The latter fall into the class of consumer grade devices, while the ADIS16448 was calibrated intrinsically by the manufacturer. The sensor unit was manufactured by Skybotix, but retrofitted with custom firmware to provide control over the filtering of inertial measurements. Both IMUs were sampled at a rate of 800 Hz. For the ADIS16448, a 2-tap filter was enabled; for the MPU9150, we chose a cut-off frequency of about 190 Hz. For exteroceptive perception, two MT9V034 WVGA global shutter image sensors were employed. The cameras were triggered at a rate of 20 Hz and set to a constant, low exposure time. We calibrated the cameras intrinsically and the stereo extrinsics using the camera calibration functionality of *kalibr* on a separate dataset beforehand.

This setup was dynamically moved by hand in front of a checkerboard of known dimensions. Subsequently, the recorded dataset was split into 20 chunks of *only* 10 s length. We ensured that all rotational degrees of freedom were excited sufficiently.

The parameters of the accelerometer and gyroscope noise models (3) and (8) were determined from static sensor data, i.e. from measurements where the IMUs were at rest. For this purpose, the sensors were mechanically fixated, and raw sensor measurements were captured at a rate of 800 Hz for a duration of 5 h. The sensor filter and range settings were identical to those used during the experiments. Table II lists the parameters that were identified and used for the experimental evaluation. Fig. 3 shows the sample Allan deviation of the gyroscopes and accelerometers, and the Allan deviation that corresponds to the selected noise model parameters.

For all experiments, we used 50 knots per second for the B-spline representing biases and 250 knots per second for the spline encoding the sensor trajectory.

TABLE II

	sym.	**unit**	**ADIS16448**	**MPU9150**
Gyroscopes				
White noise str.	σ_{ω}	$^{\circ}\,\mathrm{h}^{-1}\,\sqrt{\mathrm{Hz}}^{-1}$	3.85×10^{1}	1.84×10^{1}
Bias diffusion	$\sigma_{b\omega}$	$\mathrm{rad\,s}^{-2}\,\sqrt{\mathrm{Hz}}^{-1}$	2.66×10^{-5}	1.08×10^{-5}
Accelerometers				
White noise str.	σ_{α}	$\mathrm{m\,s}^{-2}\,\sqrt{\mathrm{Hz}}^{-1}$	1.86×10^{-3}	2.24×10^{-3}
Bias diffusion	$\sigma_{b\alpha}$	$\mathrm{m\,s}^{-3}\,\sqrt{\mathrm{Hz}}^{-1}$	4.33×10^{-4}	7.53×10^{-5}

B. IMU intrinsics and the extrinsics of multiple IMUs can be precisely inferred in a single estimator

For the experiment on extrinsic calibration of multiple IMUs, measurements of the two MPU9150 devices were employed. We defined $\underrightarrow{\mathcal{F}}_B$ to align with one of the devices and included IMU intrinsics—$\mathbf{S}_{\alpha,\omega}$,$\mathbf{M}_{\alpha,\omega}$ and $\mathbf{A}_{\omega}$—for both sensors, as well as extrinsics—$\mathbf{C}_{AB}^{\alpha,\omega}$ and ${}_B\mathbf{r}_{BA}$—into the estimator. The displacement between the IMUs was estimated as ${}_B\mathbf{r}_{BA} = [-5.98, 120.4, -1.02]^T$ mm with standard deviation of $\boldsymbol{\sigma} = [1.44, 0.67, 1.20]$ mm. These values compare well with those determined through measuring by hand ($[-10.0, 121.0, 0.0] \pm [8.0, 8.0, 0.0]$ mm). Note that the displacement between the centroids of the packages was measured, and that the uncertainty bounds (given by the package dimensions of 4×4 mm and the relative orientations of the two devices) reflect our lack of knowledge about the accurate position of the accelerometer axes inside the device. Due to imperfections in soldering devices to the printed

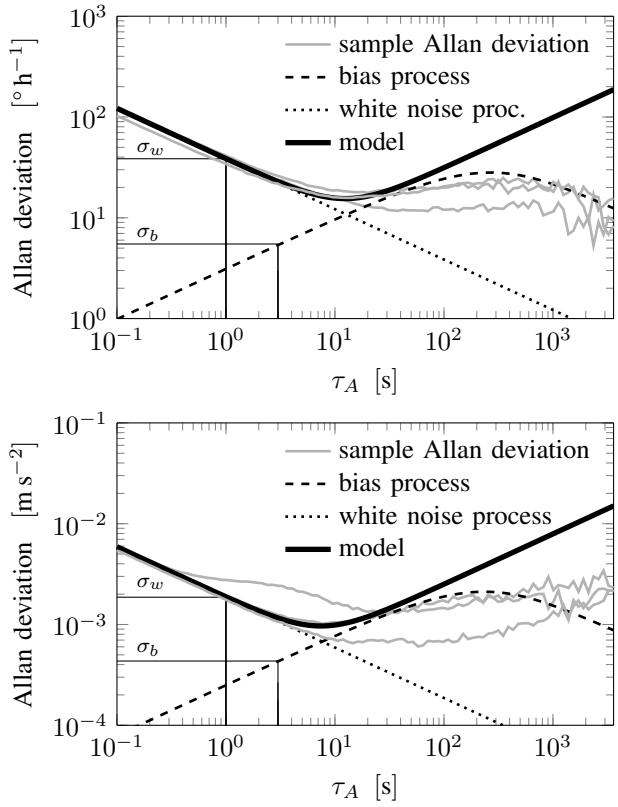

Fig. 3: Allan deviation of the MPU9150 gyroscopes (top) and accelerometers (bottom). The sample Allan deviations are shown in grey, and the Allan deviations corresponding to the noise model parameters used during the experiments are shown in black (solid).

circuit board (PCB) and in the mechanical mount connecting the PCBs holding both MPU9150 IMUs, it is impossible to acquire accurate reference measurements for the relative orientation of the two devices. Instead, we assessed the precision as the square root of the orientation variance with respect to the Fréchet expectation [22]. For $\mathbf{C}_{AB}^{\omega}$, this was evaluated to about $0.01°$, for $\mathbf{C}_{AB}^{\alpha}$ to $1.95°$. Note that absolute accuracy cannot be inferred from this assessment. While the relative orientation of the gyroscopes to the IRA exhibits a small variance, the estimate of the orientation of the accelerometers is noticeably less precise.

To ensure comparability between devices, we repeated the experiment to demonstrate intrinsic calibration for a single MPU9150 and for the ADIS16448. The estimation results for $\mathbf{S}_{\alpha,\omega}$,$\mathbf{M}_{\alpha,\omega}$ and d_c are summarized in Table III. While the ADIS16448 appears to be well calibrated by the manufacturer, significant gyroscope scale factor errors and axes misalignments were estimated for the MPU9150 (up to $1\,\%$ and $1°$). For both IMUs, a device intrinsic time delay of approximately $3\,\text{ms}$ was estimated. Over the 20 datasets, the standard deviation in the estimates were only about $15\,\mu\text{s}$ and $20\,\mu\text{s}$ respectively.

TABLE III

symbol	unit	ADIS16448	MPU9150
Accelerometer			
$\mathbf{S}_\alpha - \mathbf{I}$	ppm	$1.73 \times 10^3 \pm 1.8 \times 10^3$	$-4.20 \times 10^3 \pm 2.9 \times 10^3$
	ppm	$-6.37 \times 10^3 \pm 4.1 \times 10^3$	$7.76 \times 10^3 \pm 1.2 \times 10^3$
	ppm	$6.60 \times 10^3 \pm 6.2 \times 10^3$	$7.92 \times 10^3 \pm 2.7 \times 10^3$
$\mathbf{M}_\alpha$	″	$-0.80 \times 10^3 \pm 0.81 \times 10^3$	$-0.17 \times 10^3 \pm 0.53 \times 10^3$
	″	$-1.77 \times 10^3 \pm 1.11 \times 10^3$	$0.85 \times 10^3 \pm 0.54 \times 10^3$
	″	$-0.11 \times 10^3 \pm 1.74 \times 10^3$	$-0.36 \times 10^3 \pm 0.44 \times 10^3$
Gyroscope			
$\mathbf{S}_\omega - \mathbf{I}$	ppm	$-1.85 \times 10^3 \pm 1.6 \times 10^3$	$3.01 \times 10^3 \pm 0.6 \times 10^3$
	ppm	$1.85 \times 10^3 \pm 1.1 \times 10^3$	$-9.29 \times 10^3 \pm 0.5 \times 10^3$
	ppm	$0.99 \times 10^3 \pm 0.3 \times 10^3$	$2.74 \times 10^3 \pm 0.2 \times 10^3$
$\mathbf{M}_\omega$	″	$-0.14 \times 10^3 \pm 0.16 \times 10^3$	$-0.31 \times 10^3 \pm 0.09 \times 10^3$
	″	$-0.14 \times 10^3 \pm 0.17 \times 10^3$	$-1.71 \times 10^3 \pm 0.18 \times 10^3$
	″	$0.03 \times 10^3 \pm 0.25 \times 10^3$	$3.13 \times 10^3 \pm 0.13 \times 10^3$
d_C	µs	$2.94 \times 10^3 \pm 20$	$3.03 \times 10^3 \pm 15$

C. Positions of individual accelerometer axes can be discerned

In this experiment, three different calibrations were performed for the ADIS16448 and one of the MPU9150: A) Assuming that scaling and misalignment errors are compensated for or negligible, a standard IMU/camera calibration was performed, B) misalignment, scale errors and the effect of linear accelerations on gyroscopes were estimated, but individually different accelerometer axis displacements were neglected, and C) a full calibration including individual axis offsets was performed.

Fig. 4 depicts the estimated accelerometer positions expressed in $\underrightarrow{\mathcal{F}}_C$ for both IMUs. We determined a rough estimate of the sensor package dimensions by hand and visualized it as gray wire frames in the figures. Crosses (×) mark the estimated position of $\underrightarrow{\mathcal{F}}_A$ for calibration A. For the ADIS16448, the estimates lie clearly within the sensor package and shows a comparatively small dispersion. For the MPU9150—which is not factory calibrated—this estimate exhibits a bias and is located outside the approximate sensor dimensions. Consequently, estimating misalignment, g-sensitivity and scale in calibration B yields improved results for this device as depicted as pluses (+) in Fig. 4b. In Fig. 4b, the measured footprint does not align perfectly with our estimates. While the reason for this could lie in biased calibrations, it is similarly plausible that the device footprint measurements are inaccurate, particularly given the complications associated with determining the origin of $\underrightarrow{\mathcal{F}}_C$. For the Analog Devices product, estimating IMU intrinsics did not yield improved precision, again suggesting that the factory calibration accurately compensates for these effects. Calibration C produced clearly separated estimates for the location of individual accelerometer axes in Fig. 4a. The x-axis was estimated to be located about a centimeter apart from the y- and z- axis. This may suggest that it is housed inside a different IC, while the other two axes may share the same die. This separation of axes is less pronounced for the Invensense product, since this IMU is a single 4×4 mm

TABLE IV

		x	y	z
ADIS16448	y-axis [mm]	5.27 ± 0.53	-11.19 ± 0.31	0.67 ± 2.00
	z-axis [mm]	2.91 ± 1.12	-11.14 ± 1.36	-1.15 ± 2.59
MPU9150	y-axis [mm]	0.71 ± 0.20	0.33 ± 0.33	0.32 ± 0.72
	z-axis [mm]	1.76 ± 0.49	-0.80 ± 0.64	0.71 ± 1.27

chip. Nevertheless, the order of axes on the device can be discerned and their approximate location can be inferred. Table IV compiles the estimates of the y- and z-axis position expressed in $\underrightarrow{\mathcal{F}}_A$. Note that $\underrightarrow{\mathcal{F}}_A$ is defined in a way that its x-axis aligns with the x-axis of the device. Estimates for both devices yielded similar precision.

D. Estimating IMU intrinsics improves camera/IMU extrinsic calibration

Fig. 4b suggests that IMU scale errors and misalignments do not only result in increased variance in the estimates, but even in noticeably biased quantities. Accordingly, intrinsic calibration should be an integral part of calibration involving low-cost devices. Fig. 5 visualizes the results of Section IV-C quantitatively for the MPU9150: Using reference measurements extracted from CAD data, we determined the accuracy of the approach. Note that the estimate of the y-axis is significantly biased when IMU intrinsics are not incorporated into the estimator. Including them yields both, higher precision and greater accuracy. Please note that the aforementioned problems regarding the acquisition of reference measurements apply here as well.

V. Conclusion

In this work, we presented an extension to the open-source calibration toolbox *kalibr* that allows for determining the extrinsics and intrinsics of multiple IMUs in a single estimator. We further demonstrated that it is feasible to infer the location of individual accelerometer axes to millimeter precision.

We believe that the significance of this contribution extends beyond the application of calibrating multiple IMUs, and we intend to further investigate this in future work:

- Neglecting the physical displacement of individual accelerometer axes in high-end IMUs yields a source of deterministic error, which might be worth addressing in applications where accuracy is crucial.
- Where multiple IMUs are available, state estimation may benefit from incorporating measurements from all devices. Recently, different approaches to continuous-time SLAM have been proposed (e.g. [23], [24]), and it would be straight-forward to extend these to consider inputs from more than one IMU.

The biggest drawback of fusing data from multiple IMUs or individually displaced accelerometer axes lies in the dependence on angular accelerations, which in most sensor suites are not sensed directly. While this work showed that the continuous-time batch estimation framework is capable of inferring reasonable angular accelerations for our calibration use-case, it remains future work to demonstrate this fact for other applications and estimation frameworks. Furthermore, we did not include temporal offsets (apart from an image delay d_c) in the estimator, and future work will estimate individual delays for different IMUs as well as for accelerometers and gyroscopes, acknowledging the fact that these may not employ filters with identical characteristics.

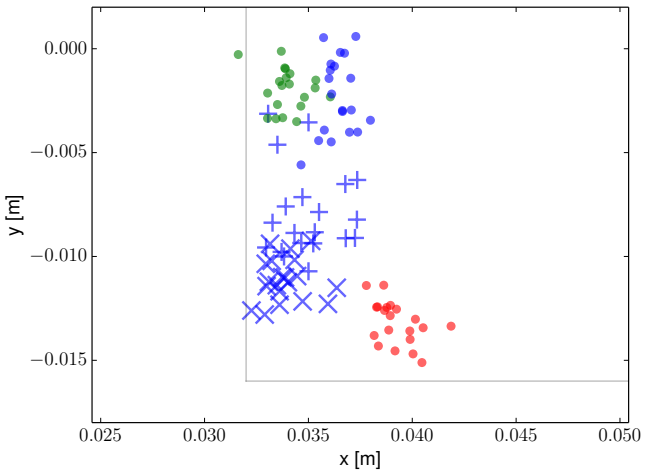

(a) ADIS16448

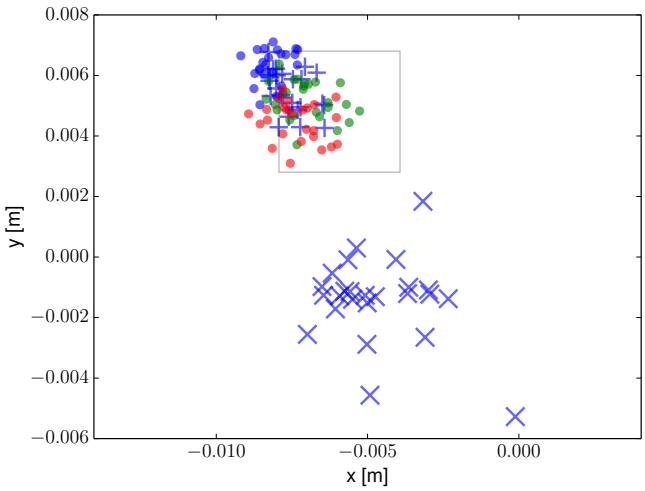

(b) MPU9150

Fig. 4: Visualization of ${}_C\mathbf{p}_{CA}$, the estimated displacement between camera and IMU. Crosses (×) mark the estimated position of $\underrightarrow{\mathcal{F}}_A$ when intrinsics are neglected (estimator A). Each cross indicates the result from one experiment. Pluses (+) visualize the position when IMU intrinsics are included in the estimation (estimator B). The results of the full-scale estimator C are indicated with dots marking the estimated position of each individual accelerometer axis (red: x-axis, green: y-axis, blue: z-axis). Results suggest that the approach is capable of discerning the positions of individual axes. The results are less pronounced for the MPU9150, where all axes are integrated in a package of 4×4 mm.

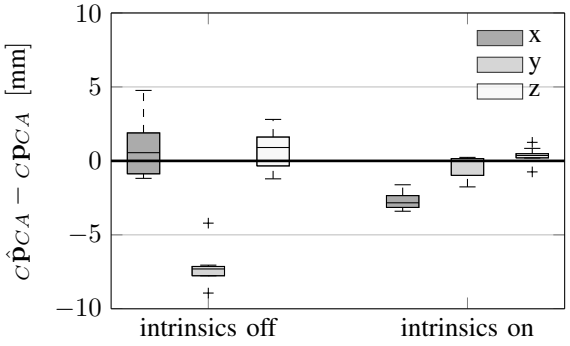

Fig. 5: Camera-IMU extrinsic translation estimation errors for experiments with the MPU9150, with and without estimating the IMU intrinsic calibration parameters. These results indicate that incorporating IMU intrinsic calibration terms improves the accuracy of the extrinsic calibration parameter estimates.

ACKNOWLEDGMENT

The authors would like to thank Paul Furgale for providing the continuous-time batch estimator framework that enabled this work, Gabriel Agamennoni for interesting discussions on the topic, and Christian Krebs for laying the groundwork for our IMU intrinsic calibration in his thesis project [15].

REFERENCES

[1] J. Ma, M. Bajracharya, S. Susca, L. Matthies, and M. Malchano, "Real-time pose estimation of a dynamic quadruped in gps-denied environments for 24-hour operation," *The International Journal of Robotics Research*, p. 0278364915587333, 2015.

[2] S. Shen, N. Michael, and V. Kumar, "Tightly-coupled monocular visual-inertial fusion for autonomous flight of rotorcraft mavs," in *Robotics and Automation (ICRA), 2015 IEEE International Conference on*. IEEE, 2015, pp. 5303–5310.

[3] S. Ovaska and S. Valiviita, "Angular acceleration measurement: a review," *Instrumentation and Measurement, IEEE Transactions on*, vol. 47, no. 5, pp. 1211–1217, Oct 1998.

[4] "Murata announces worlds first surface mount MEMS angular acceleration sensor," http://www.murata.com/en-us/about/newsroom/news/product/sensor/2015/0805, accessed 15. February 2016.

[5] P. T. Furgale, T. D. Barfoot, and G. Sibley, "Continuous-time batch estimation using temporal basis functions," in *Proceedings of the IEEE International Conference on Robotics and Automation (ICRA)*, St. Paul, MN, 14-18 May 2012, pp. 2088–2095.

[6] J. Hung, J. Hunter, W. Stripling, and H. White, "Size effect on navigation using a strapdown IMU," U.S. Army Missile Research and Development Command, Guidance and Control Directorate Technology Laboratory, Tech. Rep., 1979.

[7] P. Furgale, J. Rehder, and R. Siegwart, "Unified temporal and spatial calibration for multi-sensor systems," in *Proc. of the IEEE/RSJ International Conference on Intelligent Robots and Systems (IROS)*, 2013.

[8] F. Mirzaei and S. Roumeliotis, "A kalman filter-based algorithm for IMU-camera calibration: Observability analysis and performance evaluation," *Robotics, IEEE Transactions on*, vol. 24, no. 5, pp. 1143–1156, 2008.

[9] J. Kelly and G. Sukhatme, "Fast relative pose calibration for visual and inertial sensors," in *Experimental Robotics*. Springer, 2009, pp. 515–524.

[10] J. Kelly, N. Roy, and G. S. Sukhatme, "Determining the time delay between inertial and visual sensor measurements," *Robotics, IEEE Transactions on*, vol. 30, no. 6, pp. 1514–1523, 2014.

[11] M. Fleps, E. Mair, O. Ruepp, M. Suppa, and D. Burschka, "Optimization based IMU camera calibration," in *Intelligent Robots and Systems (IROS), 2011 IEEE/RSJ International Conference on*. IEEE, 2011, pp. 3297–3304.

[12] E. Mair, M. Fleps, M. Suppa, and D. Burschka, "Spatio-temporal initialization for IMU to camera registration," in *Robotics and Biomimetics (ROBIO), 2011 IEEE International Conference on*. IEEE, 2011, pp. 557–564.

[13] D. Zachariah and M. Jansson, "Joint calibration of an inertial measurement unit and coordinate transformation parameters using a monocular camera," in *Indoor Positioning and Indoor Navigation (IPIN), 2010 International Conference on*. IEEE, 2010, pp. 1–7.

[14] M. Li, H. Yu, X. Zheng, and A. I. Mourikis, "High-fidelity sensor modeling and calibration in vision-aided inertial navigation," in *Proceedings of the IEEE International Conference on Robotics and Automation*, Hong Kong, May 2014, pp. 409–416.

[15] C. Krebs, "Generic imu-camera calibration algorithm: Influence of imu-axis on each other," Autonomous Systems Lab, ETH Zurich, Tech. Rep., 2012. [Online]. Available: http://students.asl.ethz.ch/upl_pdf/396-report.pdf

[16] M. E. Pittelkau, "Calibration and attitude determination with redundant inertial measurement units," *Journal of Guidance, Control, and Dynamics*, vol. 28, no. 4, pp. 743–752, 2005.

[17] M. Hwangbo, J.-S. Kim, and T. Kanade, "Imu self-calibration using factorization," *Robotics, IEEE Transactions on*, vol. 29, no. 2, pp. 493–507, 2013.

[18] J.-O. Nilsson, I. Skog, and P. Handel, "Aligning the forceseliminating the misalignments in imu arrays," *Instrumentation and Measurement, IEEE Transactions on*, vol. 63, no. 10, pp. 2498–2500, 2014.

[19] P. C. Hughes, *Spacecraft Attitude Dynamics*. New York: John Wiley & Sons, 1986.

[20] J. Nocedal and S. J. Wright, *Numerical Optimization*, 2nd ed. Springer, 2006.

[21] J. Nikolic, J. Rehder, M. Burri, P. Gohl, S. Leutenegger, P. T. Furgale, and R. Siegwart, "A synchronized visual-inertial sensor system with fpga pre-processing for accurate real-time slam," in *Robotics and Automation (ICRA), 2014 IEEE International Conference on*. IEEE, 2014.

[22] X. Pennec, "Probabilities and statistics on riemannian manifolds: Basic tools for geometric measurements." in *NSIP*, 1999, pp. 194–198.

[23] S. Anderson, K. MacTavish, and T. D. Barfoot, "Relative continuous-time slam," *The International Journal of Robotics Research*, p. 0278364915589642, 2015.

[24] A. Patron-Perez, S. Lovegrove, and G. Sibley, "A spline-based trajectory representation for sensor fusion and rolling shutter cameras," *International Journal of Computer Vision*, pp. 1–12, 2015.